Supplementary Information for:

Wider Winter Temperature Variability Fuels Stronger Spring Dust Storms

Weiqi Tang[1], Yuzhi Liu[1,2,3*], Linxia Wang[1], Ying Wang[1], Yangyang Huang[1], Jie Gao[1], Dan Li[1]

[1] *College of Atmospheric Science, Lanzhou University, Lanzhou, China*

[2] *Collaborative Innovation Center on Forecast and Evaluation of Meteorological Disasters, Nanjing University of Information Science and Technology, Nanjing, China*

[3] *Research Institute of Lanzhou University in Shenzhen, Shenzhen, China*

Corresponding author: Yuzhi Liu, liuyzh@lzu.edu.cn

This Supplementary Materials file includes:

Supplementary Text
Figures S1 to S9
Tables S1 to S2

Supplementary Text

S1. Definition of global dust source (GDS) and dust transport regions

In this study, the identified bare soil areas are considered potential dust source regions, whereas all other regions are classified as dust transport regions. Bare soil areas are identified using the multi-year (2001–2020) mean International Geosphere-Biosphere Programme (IGBP) land-cover classification, derived from the Moderate-resolution Imaging Spectroradiometer (MODIS).

S2. Classification of Preceding-winter Temperature Characteristics

To investigate the influence of preceding-winter temperature characteristics on following-spring dust activity, we classified winters from 1979 to 2023 according to their thermal conditions. The winter season is defined as December-January-February (DJF) for the Northern Hemisphere and June–July–August (JJA) for the Southern Hemisphere. The minimum hourly 2-m air temperature within each day is defined as the daily minimum 2-m air temperature (T_{min}). All analyses are based on the daily T_{min} from the ERA5 reanalysis dataset, spatially averaged over major GDS regions.

First, to categorize winters by mean T_{min}, we calculate the winter-mean T_{min} for each winter over GDS regions. The resulting 45-year time series is ranked in ascending order. Winters falling within the lowest 30% of this ranking are classified as anomalously cold winters (referred to in the manuscript as cold winters), while those in the highest 30% are classified as anomalously warm winters (referred to in the manuscript as warm winters).

Second, to quantify winter temperature variability, we calculate the standard deviation of daily T_{min} for each winter. The standard deviation of daily T_{min} is calculated for each winter as follows: calculate the standard deviation of T_{min} for each winter (a total of 90 or 91 days) using the following formula:

$$\sigma_y = \sqrt{\frac{\sum_{i=1}^{N}(x_i-\mu)^2}{N}} \tag{1}$$

Where y denotes the year index from 1979 to 2023. N represents the number of daily samples in each winter. x_i denotes area-averaged T_{min} over GDS regions. μ represents the seasonal mean T_{min} for each winter over GDS regions. The resulting standard deviation time series is linearly detrended to remove the long-term trend while retaining interannual fluctuations. Following the same ranking procedure, winters in the lowest and highest 30% of the detrended series are defined as low-variability winters and high-variability winters, respectively.

S3. Cumulative distribution function (CDF) analysis

To characterize the probability distribution of dust storm days under different climatic conditions, we employ the cumulative distribution function (CDF). The CDF is defined as:

$$\mathrm{F(x) = P(X \leq x)} \tag{2}$$

where $\mathrm{P}(X \leq x)$ is the cumulative probability that a random variable X takes a value less than or equal to a specific threshold x. Unlike summary metrics such as the mean and standard deviation, the CDF incorporates the full sample distribution[1]. The CDF therefore characterizes not only shifts in central tendency but also changes in distributional spread and the probability of extremes (i.e., tail probabilities).

The CDFs are constructed as follows. For each winter category (e.g., cold winters), all corresponding dust storm day frequencies are collected and ranked in ascending order. These ranked data are then divided into 25 bins to calculate the probability density for each bin. The cumulative probability for any given bin is then computed by cumulatively summing the probability densities of all bins up to and including that bin. We apply this procedure to construct CDFs for dust storm days during both cold and warm winters, for the global dataset and individual GDS regions separately.

Comparison of the resulting CDFs allows a quantitative assessment of shifts in the statistical distribution of dust storm activity between cold and warm winters. This approach provides a comprehensive assessment for diagnosing how different thermal conditions impact both typical and extreme dust storm activity.

S4. Calculation of stream function

In order to understand the oceanic influence on the dust storms, we calculate the T-N wave activity flux (WAF) to analyze energy propagation[2,3]. The specific method is as follows[4]:

$$F_x = \frac{pcos\varphi}{2|U|}\left\{\frac{U}{a^2cos^2\varphi}\left[\left(\frac{\partial\psi'}{\partial\lambda}\right)^2 - \psi'\frac{\partial^2\psi'}{\partial\lambda^2}\right] + \frac{V}{a^2cos\varphi}\left[\frac{\partial\psi'}{\partial\lambda}\frac{\partial\psi'}{\partial\varphi} - \psi'\frac{\partial^2\psi'}{\partial\lambda\partial\varphi}\right]\right\} \quad (3)$$

$$F_y = \frac{pcos\varphi}{2|U|}\left\{\frac{U}{a^2cos\varphi}\left[\frac{\partial\psi'}{\partial\lambda}\frac{\partial\psi'}{\partial\varphi} - \psi'\frac{\partial^2\psi'}{\partial\lambda\partial\varphi}\right] + \frac{V}{a^2}\left[\left(\frac{\partial\psi'}{\partial\lambda}\right)^2 - \psi'\frac{\partial^2\psi'}{\partial\varphi^2}\right]\right\} \quad (4)$$

$$F_z = \frac{pcos\varphi}{2|U|}\left\{\frac{f_0^2}{N^2}\frac{U}{acos\varphi}\left[\frac{\partial\psi'}{\partial\lambda}\frac{\partial\psi'}{\partial z} - \psi'\frac{\partial^2\psi'}{\partial\lambda\partial z}\right] + \frac{V}{a}\left[\frac{\partial\psi'}{\partial\lambda}\frac{\partial\psi'}{\partial z} - \psi'\frac{\partial^2\psi'}{\partial\lambda\partial z}\right]\right\} \quad (5)$$

Where F_x and F_y denote horizontal WAF. F_z represents vertical WAF. $\varphi,\ \lambda,\ z,\ a, p$ represent latitude, longitude, geopotential height, Earth's radius, and pressure respectively. $\psi' = \frac{\Phi'}{f_0}$ is the perturbation of the quasi-geostrophic flow function relative to the basic flow field, and Φ represents the geopotential height field. f_0 represents the Coriolis parameter. The $U = (U, V)$ is the basic flow field. In this study, the difference in geopotential height field between high- and low- variability winters is considered the Φ'. Besides, the averaged wind field from 1979 to 2023 is considered the basic flow field.

S5. Random Forest (RF) model configuration and predictor selection

To evaluate the predictive value of the identified preceding-winter climate signals, we employ the Random Forest (RF) algorithm. RF is selected because it performs well with relatively small sample sizes, can capture nonlinear relationships and interactions among predictors, and is less sensitive to multicollinearity and overfitting than many conventional statistical approaches[5]. The model is trained using preceding-winter predictors derived from the physical mechanisms identified in this study. Model robustness is assessed using a leave-one-out cross-validation (LOOCV) framework. Although LOOCV maximizes the use of the available samples, previous methodological studies have shown that its estimates of predictive performance may be optimistic for small datasets[6,7]. Therefore, five-fold cross-validation is additionally performed to provide a complementary assessment of model generalization. The complete dataset is randomly divided into five approximately equal subsets, each containing nine years of data. In each iteration, four subsets are used for model training and the remaining subset is reserved for validation, with the process repeated until each subset serves once as the validation set.

To examine the sensitivity of the RF model to model configuration and predictor selection, a series of sensitivity experiments is conducted. Model performance is compared across two tree depths (*max depth* = 2 and *max depth* = None) under both the LOOCV and five-fold cross-validation frameworks. Different combinations of preceding-winter predictors, including T_{min} variability, large-scale circulation indices (the NAO and AO indices), soil moisture (SM1 and SM2), and surface sensible heat flux (HF), are evaluated. Model skill is quantified using the correlation between the spatially averaged predicted spring DAOD and the corresponding MERRA-2 DAOD time series (Supplementary Fig. S8). Among all configurations, the model using *max depth* = None together with the predictor combination of SM1, SM2 and HF achieves the highest correlation with MERRA-2. Comparable performance under the LOOCV and five-fold cross-validation frameworks further demonstrates that the predictive skill is robust and insensitive to the choice of validation strategy.

Interestingly, introducing NAO in addition to T_{min} variability does not further improve the prediction skill (Supplementary Fig. S8). This suggests that much of the predictive information associated with large-scale atmospheric circulation is already encapsulated by preceding-winter T_{min} variability. This interpretation is consistent with the physical mechanism proposed in this study, whereby large-scale circulation influences spring dust activity primarily through its modulation of preceding-winter temperature variability. Similarly, models driven only by land-surface variables (soil moisture and sensible heat flux) outperform those that additionally included preceding-winter T_{min} variability. This suggests that much of the predictive information contained in T_{min} variability is already encapsulated in the subsequent land-surface state through the persistence of soil moisture and thermal anomalies. These results closely mirror the proposed ocean-atmosphere-land pathway and provide an independent machine-learning validation of the underlying physical mechanism.

Feature importance is further assessed using permutation importance (Supplementary Fig. S8b), which estimates the contribution of each predictor by measuring the reduction in model performance after randomly permuting an individual predictor while leaving all remaining predictors unchanged. Both the LOOCV and five-fold cross-validation frameworks produce a consistent ranking of predictor importance, with SM1 contributing the most, followed by SM2 and HF. The agreement between the two validation strategies indicates that the estimated predictor importance is robust to the choice of cross-validation scheme. Moreover, the dominance of soil moisture variables is consistent with the proposed land-memory mechanism, highlighting persistent soil moisture anomalies as the dominant source of predictive information linking preceding-winter climate variability to subsequent spring dust activity.

S6. Reanalysis data employed in this study

This study uses the fifth-generation European Centre for Medium-Range Weather Forecasts (ECMWF) reanalysis (ERA5) to investigate land-surface and atmospheric conditions over GDS areas and their relationship with spring dust activity. ERA5 has a spatial resolution of $0.25° \times 0.25°$, providing globally consistent and continuous long-term atmospheric and land-surface information. From ERA5, hourly T_{min} for the preceding winter from 1979 to 2023 is calculating daily T_{min} (see Supplementary Text S2 for details), which used to characterize near-surface thermal anomalies. Monthly mean spring soil moisture and soil temperature from 1980 to 2024 (hereafter following spring, defined as March–May in the Northern Hemisphere and September–November in the Southern Hemisphere) are used to represent land-surface conditions. Soil moisture and soil temperature are analyzed at four soil layers (0–7 cm, 7–28 cm, 28–100 cm, and 100–289 cm). Near-surface dynamic conditions are represented by 10-m winds, and land-atmosphere turbulent heat exchange is characterized by surface sensible heat fluxes.

Dust aerosol data are obtained from the Modern-Era Retrospective Analysis for Research and Applications, Version 2 (MERRA-2) reanalysis dataset produced by the Global Modeling and Assimilation Office (GMAO) of the National Aeronautics and Space Administration (NASA). This study uses monthly mean MERRA-2 data for the following spring, including dust aerosol optical depth (DAOD), dust column mass density (referred to in the manuscript as dust loading), and near-surface dust mass concentration. DAOD represents the column-integrated optical effect of dust aerosols in the atmosphere. Dust loading quantifies the total dust mass per unit atmospheric column. Near-surface dust mass concentration characterizes the spatiotemporal variability of dust particles in the near-surface layer. MERRA-2 has a spatial resolution of $0.5° \times 0.625°$ and is used to investigate long-term variations in dust activity and their relationships with preceding-winter climate anomalies.

To illustrate the mechanism underlying ocean-atmosphere-land, the global daily multi-layer data of wind field and geopotential height derived from the National Oceanic and Atmospheric Administration (NOAA) Physical Sciences Laboratory (PSL) are used to calculate the stream function. These data are available from 1979 to 2023, with a horizontal resolution of 2.5 °×2.5 °, and a total of 17 pressure layers selected vertically from 1000 to 10 hPa.

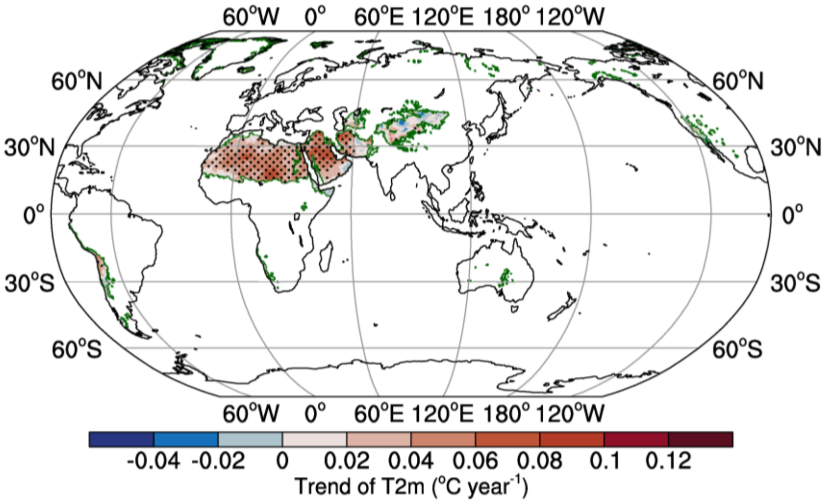

Fig. S1. Long-term trends in preceding-winter minimum 2-m temperature (T_{min}). Spatial distribution of the linear trend in previous-winter T_{min} over global dust source (GDS) areas from 1979 to 2023. Black dots indicate trends significant at the 95% confidence level. Green outlines delineate major GDS regions.

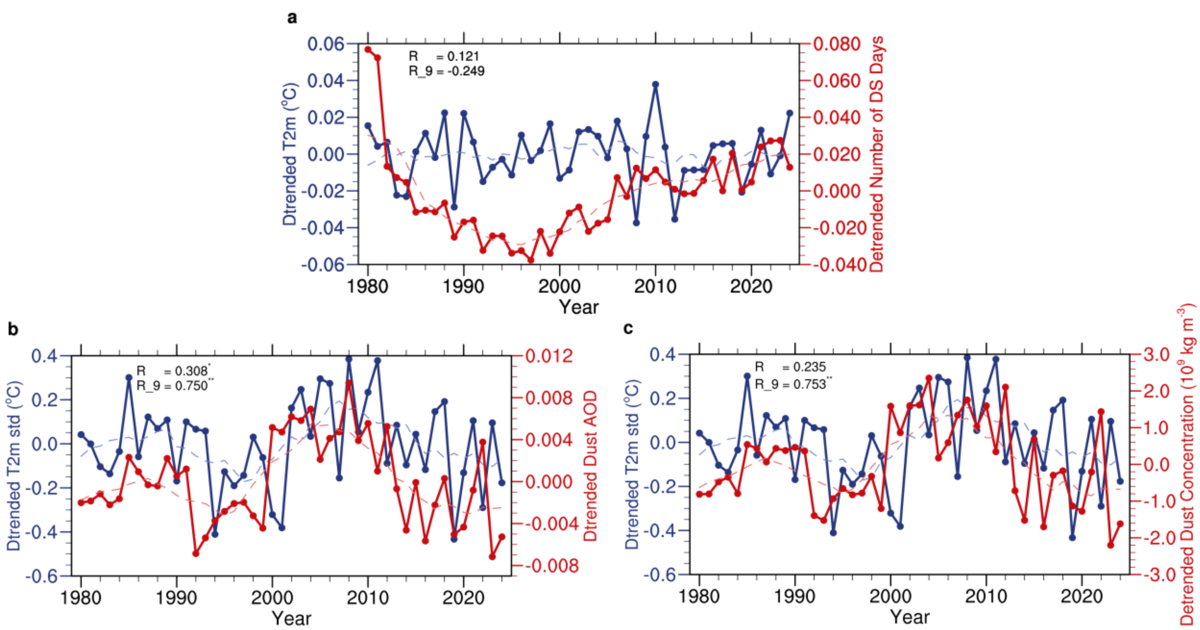

Fig. S2. Relationships between preceding-winter T_{min} characteristics and dust activity. (a) Temporal relationship between the detrended preceding-winter T_{min} over GDS areas and detrended global dust storm frequency in the following spring. Temporal relationships between the detrended preceding-winter T_{min} variability over GDS areas and detrended global (b) dust aerosol optical depth (DAOD) and (c) surface dust mass concentration (10^9 kg m^{-3}) in the following spring. Dashed lines denote the 9-point running means. Single (*) and double (**) asterisks indicate significance at the 90% and 95% confidence levels, respectively.

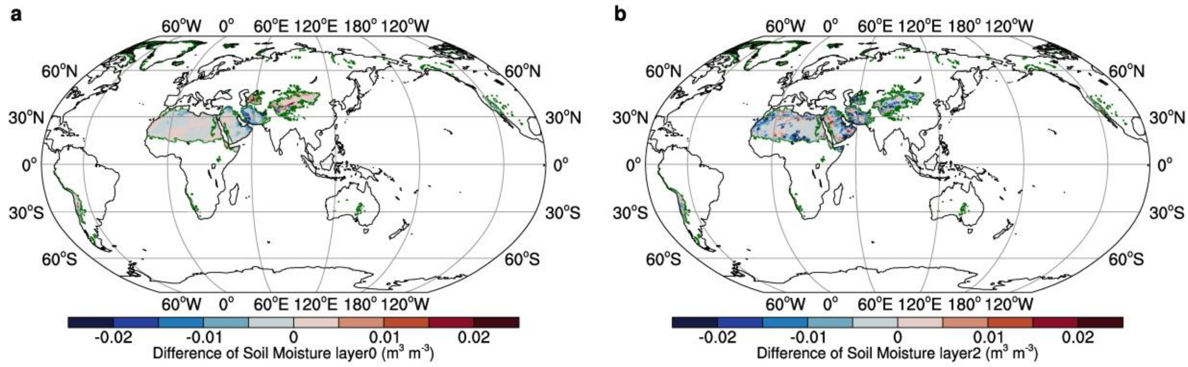

Fig S3. Composite differences in soil moisture (m^3 m^{-3}) during the following-spring over GDS areas between high- and low-variability winters. Soil moisture at (a) 0–7 cm depth and (b) 28–100 cm depth. Green outlines delineate major GDS regions.

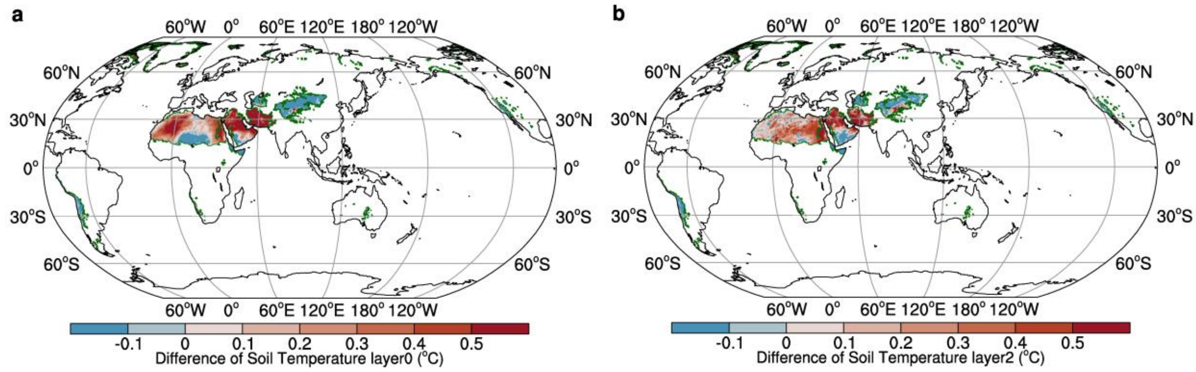

Fig. S4. Composite differences in following-spring soil temperature (℃) over GDS areas between high- and low-variability winters. Soil temperature at (a) 0–7 cm depth and (b) 28–100 cm depth. Green outlines delineate major GDS regions.

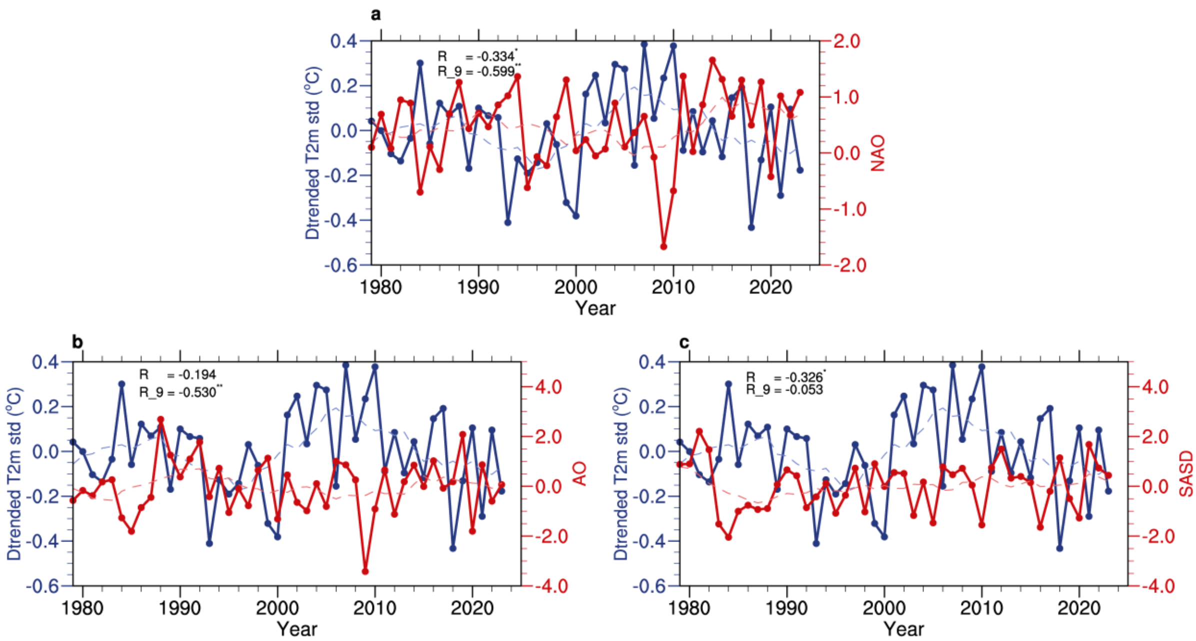

Fig. S5. Time series of the detrended standard deviation of previous-winter T_{min} (blue line) in GDS areas and the (a) the North Atlantic Oscillation (NAO, red line), (b) Arctic Oscillation (AO, red line), and (c) South Atlantic Subtropical Dipole (SASD, red line) in the following spring. Dashed lines represent the 9-point running mean, Single

(*) and double (**) asterisks indicate significance at the 90% and 95% confidence levels, respectively.

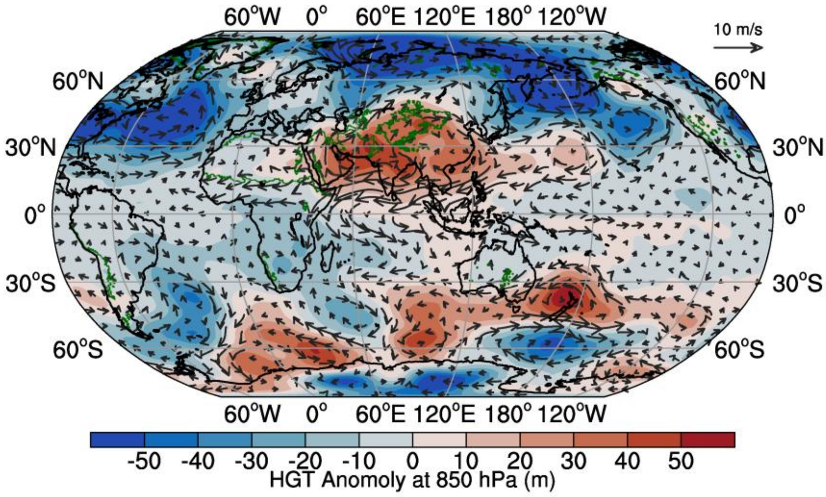

Fig. S6. Differences in 850-hPa geopotential height (m; shading) and wind vectors (m s^{-1}; arrows) between high- and low-variability winters. Green outlines delineate major GDS regions.

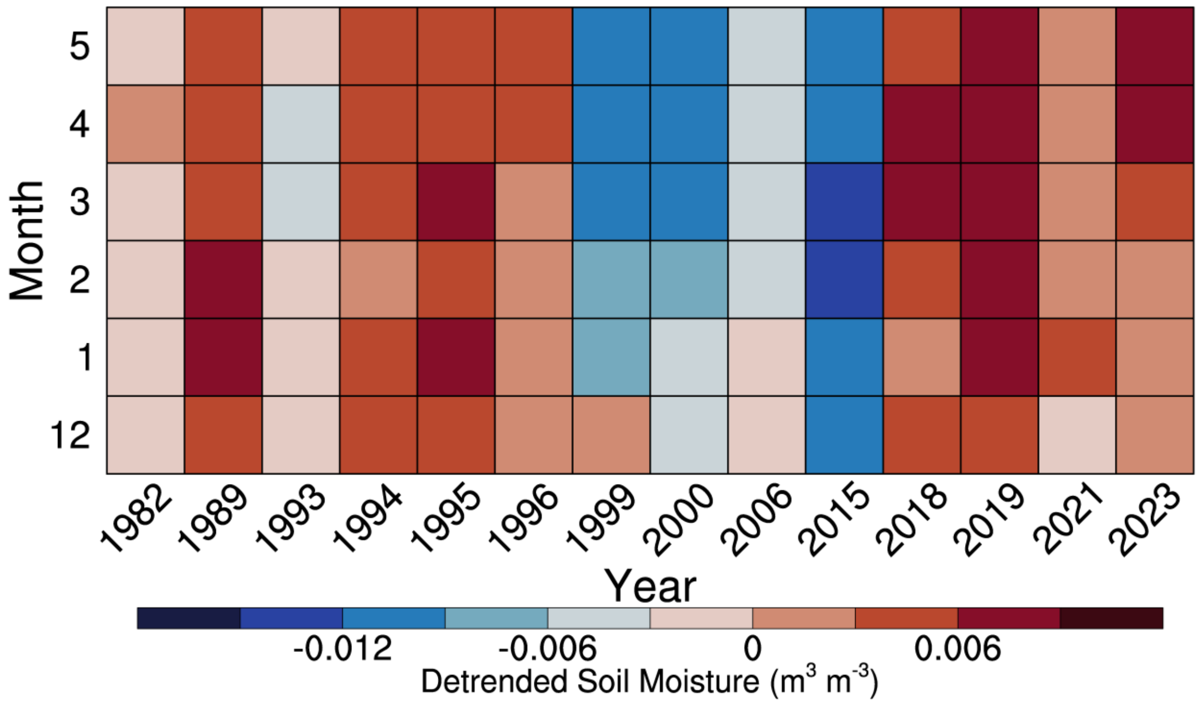

Fig. S7. Monthly evolution of detrended soil moisture (m^3 m^{-3}) over GDS areas from the preceding winter to following spring during low-variability winters.

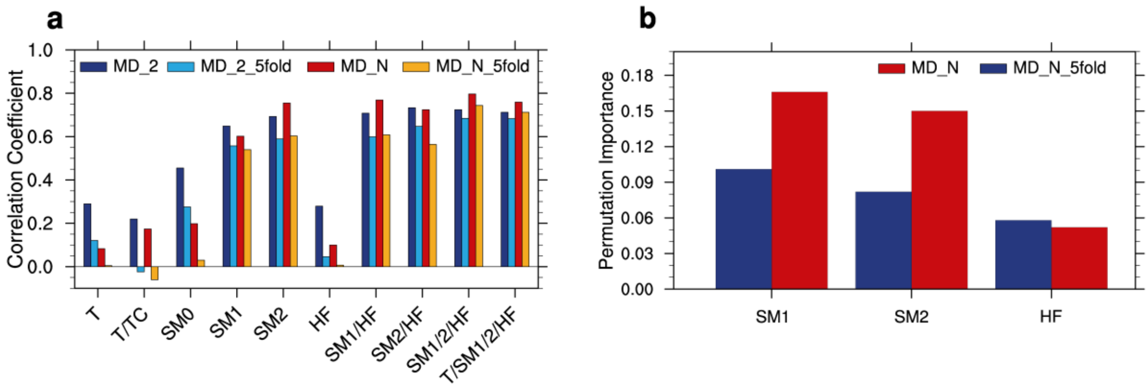

Fig. S8. Sensitivity analysis of Random Forest (RF) model configuration and predictor selection. (a) Correlation coefficients between the spatially averaged spring dust aerosol optical depth (DAOD) predicted by the RF model and the corresponding MERRA-2 DAOD under different model configurations. Four bars are shown for each predictor combination, representing models with *max depth* = 2 and *max depth* = None, each evaluated using leave-one-out cross-validation (LOOCV) and five-fold cross-validation. T denotes preceding-winter T_{min} variability. TC denotes the large-scale circulation indices (the NAO and AO). SM0, SM1, SM2 denote soil moisture at depths of 0–7cm, 7–28cm, 28–100cm, respectively. HF indicates surface sensible heat flux. **(b)** Relative importance of the optimal predictor set estimated using permutation importance. Blue and red bars represent feature importance estimated using LOOCV and five-fold cross-validation, respectively.

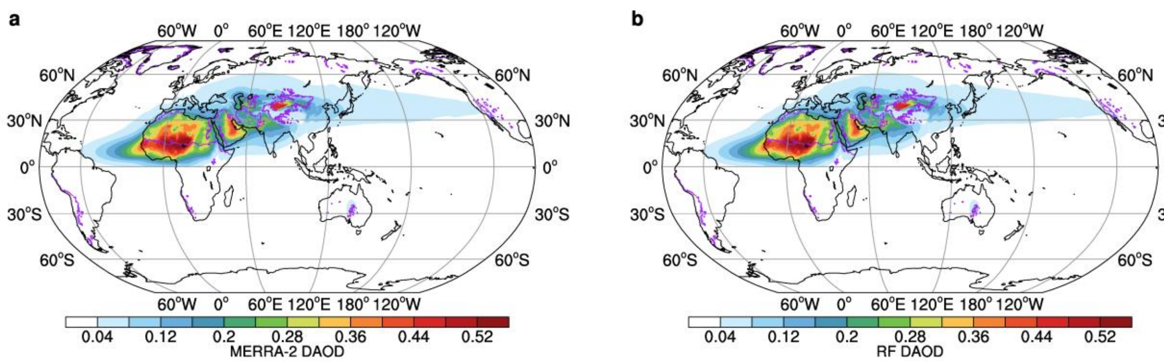

Fig. S9. Spatial distributions of (a) MERRA-2 DAOD and (b) RF-predicted DAOD. Purple outlines delineate major GDS regions.

Table S1. Classification of cold/warm winters and low-/high-variability winters based on preceding-winter T_{min} over GDS areas.

Criterion	Category	Years
Minimum 2-m temperature	Cold winters	1980, 1981, 1982, 1983, 1984, 1986, 1988, 1991, 1992, 1993, 1994, 1999, 2007, 2011
	Warm winters	1998, 2001, 2002, 2005, 2008, 2009, 2010, 2015, 2016, 2017, 2019, 2020, 2022, 2023

Temperature variability	Low-variability winters	1982, 1989, 1993, 1994, 1995, 1996, 1999, 2000, 2006, 2015, 2018, 2019, 2021, 2023
	High-variability winters	1984, 1986, 1988, 1990, 2001, 2002, 2004, 2005, 2007, 2009, 2010, 2016, 2017, 2020

References

1. Luo, Y. et al. An improved statistical bias correction method for Global Climate Model (GCM) precipitation projection: A case study on the CMCC-CM2-SR5 model projection in China's Huaihe River Basin. *J. Hydrol. Reg. Stud.* **57**, 102146 (2025).
2. Tam, C. Y. & Li, T. The origin and dispersion characteristics of the observed tropical summertime synoptic-scale waves over the western Pacific. *Mon. Weather Rev.* **134**, 1630–1646 (2006).
3. Miao, R., Wen, M., Zhang, R. & Li, L. The influence of wave trains in mid-high latitudes on persistent heavy rain during the first rainy season over South China. *Clim. Dyn.* **53**, 2949–2968 (2019).
4. Takaya, K. & Nakamura, H. A formulation of a phase-independent wave-activity flux for stationary and migratory quasigeostrophic eddies on a zonally varying basic flow. J. Atmos. Sci. 58, 608–627 (2001).
5. Breiman, L. Random forests. *Mach. Learn.* **45**, 5–32 (2001).
6. Kohavi, R. A study of cross-validation and bootstrap for accuracy estimation and model selection. *In Proceedings of the 14th International Joint Conference on Artificial Intelligence (IJCAI)* (1995).
7. Geroldinger, A. Lusa, L., Nold, M. & Heinze, G. Leave-one-out cross-validation, penalization, and differential bias of some prediction model performance measures—a simulation study. *Diagn. Progn. Res.* **7**, 9 (2023).